Title

Imaging the dynamic recruitment of monocytes to the blood—brain barrier and specific brain regions during Toxoplasma gondii infection

Journal

Proceedings of the National Academy of Sciences of the United States of America, 116(49)

ISSN

0027-8424

Authors

Schneider, Christine A
Velez, Dario X Figueroa
Azevedo, Ricardo
et al.

Publication Date

2019-12-03

DOI

10.1073/pnas.1915778116

Peer reviewed

Imaging the dynamic recruitment of monocytes to the blood–brain barrier and specific brain regions during *Toxoplasma gondii* infection

Christine A. Schneider[a,b], Dario X. Figueroa Velez[c,1], Ricardo Azevedo[c,1], Evelyn M. Hoover[a,b], Cuong J. Tran[a,b], Chelsie Lo[c], Omid Vadpey[a,b], Sunil P. Gandhi[c,d], and Melissa B. Lodoen[a,b,2]

[a]Department of Molecular Biology and Biochemistry, University of California, Irvine, CA 92697; [b]Institute for Immunology, University of California, Irvine, CA 92697; [c]Department of Neurobiology and Behavior, University of California, Irvine, CA 92697; and [d]Center for the Neurobiology of Learning and Memory, University of California, Irvine, CA 92697

Edited by L. David Sibley, Washington University in St. Louis, St. Louis, MO, and approved October 6, 2019 (received for review September 15, 2019)

Brain infection by the parasite *Toxoplasma gondii* in mice is thought to generate vulnerability to predation by mechanisms that remain elusive. Monocytes play a key role in host defense and inflammation and are critical for controlling *T. gondii*. However, the dynamic and regional relationship between brain-infiltrating monocytes and parasites is unknown. We report the mobilization of inflammatory (CCR2^{+}Ly6C^{hi}) and patrolling (CX3CR1^{+}Ly6C^{lo}) monocytes into the blood and brain during *T. gondii* infection of C57BL/6J and CCR2$^{RFP/+}$CX3CR1$^{GFP/+}$ mice. Longitudinal analysis of mice using 2-photon intravital imaging of the brain through cranial windows revealed that CCR2-RFP monocytes were recruited to the blood–brain barrier (BBB) within 2 wk of *T. gondii* infection, exhibited distinct rolling and crawling behavior, and accumulated within the vessel lumen before entering the parenchyma. Optical clearing of intact *T. gondii*-infected brains using iDISCO^{+} and light-sheet microscopy enabled global 3D detection of monocytes. Clusters of *T. gondii* and individual monocytes across the brain were identified using an automated cell segmentation pipeline, and monocytes were found to be significantly correlated with sites of *T. gondii* clusters. Computational alignment of brains to the Allen annotated reference atlas [E. S. Lein et al., *Nature* 445:168–176 (2007)] indicated a consistent pattern of monocyte infiltration during *T. gondii* infection to the olfactory tubercle, in contrast to LPS treatment of mice, which resulted in a diffuse distribution of monocytes across multiple brain regions. These data provide insights into the dynamics of monocyte recruitment to the BBB and the highly regionalized localization of monocytes in the brain during *T. gondii* CNS infection.

monocyte | *Toxoplasma gondii* | CNS infection | LPS | blood–brain barrier

Monocytes are innate immune cells with phagocytic and cytokine-producing functions that contribute to host defense and inflammation (1). They originate in the bone marrow from a common myeloid progenitor and circulate in the blood during homeostasis (2, 3). Monocytes play a role in noninfectious inflammatory conditions, such as atherosclerosis and autoimmune diseases, and also participate in early host defense against bacterial, viral, and eukaryotic pathogens (4). During infection, monocytes are mobilized from the bone marrow and into tissues, and in many cases are recruited by the chemokine CCL2, which signals through the monocyte chemokine receptor CCR2 (5, 6). Functionally, monocytes phagocytose cellular debris and pathogens, release pro- and antiinflammatory cytokines, and even direct T cell priming and polarization (7).

Monocytes in mice are classified into 2 subsets based on differential function and expression of cell-surface immune receptors (8). In mice, "inflammatory" monocytes express high levels of Ly6C and CCR2, and these cells are the canonical progenitors to tissue macrophages and dendritic cells following recruitment to sites of inflammation (9, 10). Conversely, "patrolling" monocytes express high levels of CX3CR1 and low levels of Ly6C. This subset was characterized based on a low-velocity crawling behavior on vascular endothelium during homeostasis and in response to tissue injury, although patrolling monocytes can also enter tissues during inflammatory events (11). The expression pattern of CCR2 and CX3CR1 on human monocyte subsets mirrors the expression on murine monocytes with similar gene expression and functional characteristics: CD14^{+}CD16^{lo} monocytes are functionally similar to murine inflammatory monocytes, and CD14^{lo}CD16^{+} monocytes are analogous to murine patrolling monocytes (12–14).

Toxoplasma gondii is a protozoan parasite that is found worldwide and is estimated to infect one-third of the human population (15). Although *T. gondii* is a food-borne pathogen, the parasite readily disseminates to many organs, including the brain, where it establishes a chronic infection that persists for the lifetime of the host (16). Active immune surveillance is critical for maintaining host control of the parasite, and immune suppression leads to reactivation of the dormant parasites and the potential for substantial central nervous system (CNS) pathology, including seizure and death (17).

While T cells have long been known to control *T. gondii* in the acute and chronic phases of infection (18), more recent evidence

Significance

Monocytes circulate in the blood and are involved in host defense, inflammation, neurodegeneration, and autoimmune disease. How and where these cells enter the brain during disease remains poorly understood. We analyzed monocyte recruitment to the brain during infection with *Toxoplasma gondii*, a global foodborne parasite that establishes chronic infection in the CNS. By using 2-photon imaging through cranial windows, we dynamically tracked fluorescent monocytes at the blood–brain barrier from the acute to chronic stage of infection in mice. Whole-brain imaging revealed distinct localization patterns of monocytes in specific brain regions and near sites of parasite infection, providing a global 3D analysis of monocytes in the brain and indicating portals of entry for immune cells to the CNS during infection.

Author contributions: C.A.S., D.X.F.V., R.A., S.P.G., and M.B.L. designed research; C.A.S., D.X.F.V., R.A., E.M.H., C.J.T., C.L., and O.V. performed research; R.A. contributed new reagents/analytic tools; C.A.S., D.X.F.V., R.A., E.M.H., and M.B.L. analyzed data; and C.A.S., D.X.F.V., R.A., E.M.H., S.P.G., and M.B.L. wrote the paper.

The authors declare no competing interest.

This article is a PNAS Direct Submission.

Data deposition: The code associated with this paper has been deposited in GitHub (https://github.com/sunilgandhilab/brainquant3d).

[1]D.X.F.V. and R.A. contributed equally to this work.

[2]To whom correspondence may be addressed. Email: mlodoen@uci.edu.

This article contains supporting information online at https://www.pnas.org/lookup/suppl/doi:10.1073/pnas.1915778116/-/DCSupplemental.

First published November 14, 2019.

suggests that myeloid cells, including monocytes, also play a key role in the immune response. During *T. gondii* infection of mice, CCR2$^+$ inflammatory monocytes are rapidly mobilized to peripheral sites of infection and are essential for survival during the acute stage of disease (19–22). Evidence also indicates a protective role for CCR2$^+$ monocytes in containing CNS pathology in mice chronically infected with *T. gondii* (23, 24). Although monocytes are present in the brain and mediate host defense during chronic *T. gondii* infection, little is known about the dynamics of trafficking and migration of monocytes from the bloodstream into the CNS or about the regional localization of these cells in the brain during infection.

We have defined the initial mobilization of monocytes into the blood and the recruitment of these cells to the CNS during *T. gondii* infection of mice. Both patrolling and inflammatory monocytes were recruited to the blood–brain barrier (BBB) in *T. gondii*-infected mice within the first 2 wk of infection. Longitudinal 2-photon imaging of the brain microvasculature revealed that monocytes exhibited distinct rolling and crawling behavior at the BBB, and interestingly, accumulated within the vessel lumen prior to transmigration into the parenchyma. Whole-brain clearing and light-sheet fluorescence microscopy (LSFM) revealed consistent patterns of monocyte infiltration, specifically in the olfactory tubercle, with a notable lack of monocyte enrichment in other regions. In contrast, lipopolysaccharide (LPS)-induced inflammation resulted in a diffuse distribution of monocytes to multiple brain regions. Collectively, these data provide insights into the dynamics of both acute and chronic inflammatory recruitment of monocytes to the brain and a global 3D analysis of monocyte localization in the brain during CNS infection and inflammation.

Results

Inflammatory and Patrolling Monocytes Increase in the Blood during Acute Infection with *T. gondii*. To determine the kinetics of monocyte mobilization into the blood, we intraperitoneally injected C57BL/6J mice with PBS as a control or with GFP-expressing *T. gondii* (type II, *Prugniaud* strain) and tracked the frequencies of immune cells in the blood at 4 and 6 d postinfection (dpi) by flow cytometry. Sequential gating of the CD45$^+$ leukocytes from the blood was used to identify lymphocytes (NK, NKT, T, and B cells), neutrophils, and monocytes. Inflammatory monocytes were identified as CD11b$^+$Ly6C^{hi}, and patrolling monocytes as CD11b$^+$Ly6C^{lo} (Fig. 1*A*), as previously reported (8). Monocytes accounted for a small percentage of the total leukocytes in the blood of PBS control mice (Fig. 1*B*), whereas the percentage of Ly6C^{hi} and Ly6C^{lo} monocytes increased by 3.3-fold and 3.1-fold, respectively, at 6 dpi in *T. gondii*-infected mice (Fig. 1*B*). There was also an increase in the frequency of NK cells and neutrophils (PMN), whereas the percentage of B cells decreased dramatically (Fig. 1*C* and *SI Appendix*, Table S1). CCL2 is the dominant ligand for the CCR2 receptor and initiates monocyte mobilization from the bone marrow into the blood. As expected, higher levels of CCL2 were observed in the sera at 4 dpi (119.1 ± 54.86 pg/mL) and 6 dpi (130.5 ± 33.4 pg/mL) compared to control mice (6.84 ± 5.11 pg/mL) (Fig. 1*D*). We also detected an increase in cytokines typically induced during acute infection with *T. gondii*, including IFN-γ and TNF-α, which increased over 5,000-fold and 6.9-fold, respectively, by 6 dpi (Fig. 1*D*).

We next evaluated monocyte recruitment to the brain during acute time points by isolating cells from brain homogenates for surface staining and flow cytometry. Monocytes were identified as CD45^{hi}CD11b$^+$ (and negative for the NK cell and neutrophil markers NK1.1 and Ly6G, respectively) and further classified based on Ly6C expression (Fig. 1*E*). Ly6C^{hi} and Ly6C^{lo} monocytes were detectable at a low level in brain homogenates by 6 dpi (Fig. 1*F*) and represented a small fraction of the overall CD45$^+$ cells, which were predominantly comprised of native microglia (CD45^{int}CD11b$^+$) at these early time points (Fig. 1*G*).

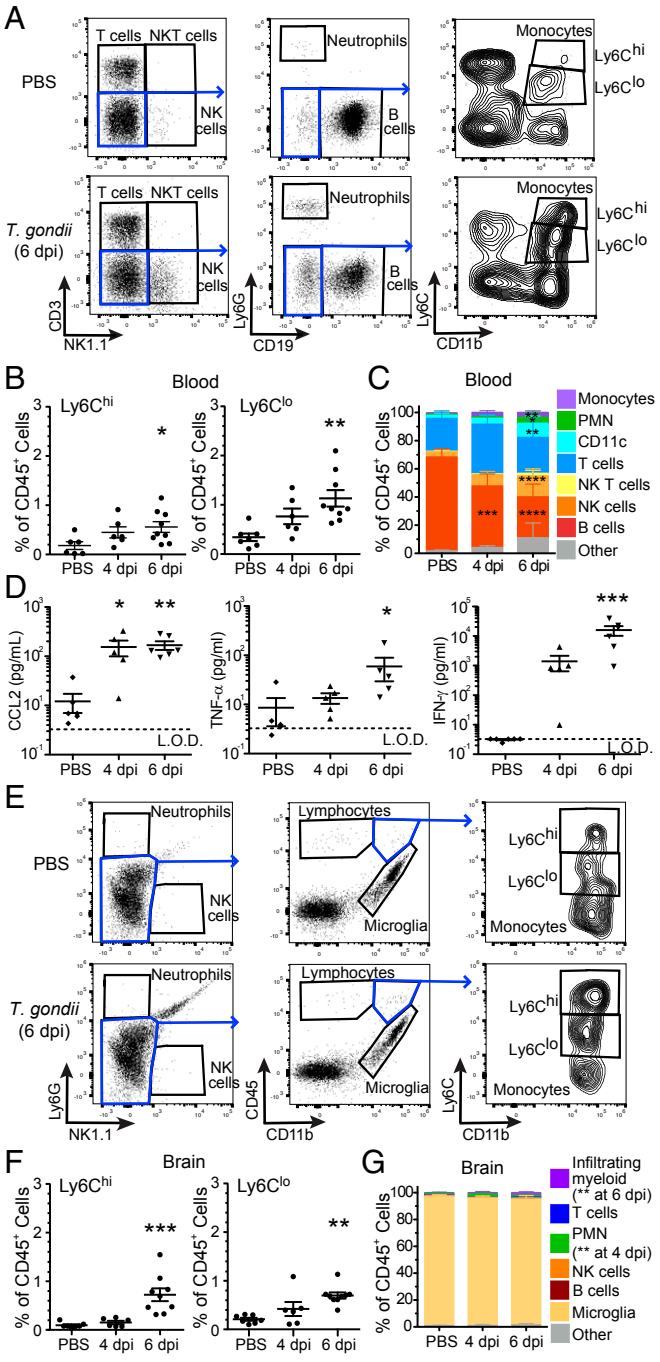

Fig. 1. Monocytes increase in the blood and are recruited to the brain during acute infection. C57BL/6J mice were infected intraperitoneally with 1,000 type II *T. gondii* or injected with PBS as a control and analyzed for immune cells in the blood and brain by flow cytometry. (*A*) Representative gating of CD45$^+$ cells from the blood of PBS-treated or *T. gondii*-infected mice. Monocytes were defined as CD45$^+$CD3$^-$NK1.1$^-$CD11b$^+$ and either Ly6C^{hi} or Ly6C^{lo}. (*B*) Frequencies of Ly6C^{hi} or Ly6C^{lo} monocytes in blood at 4 and 6 dpi. (*C*) Dominant immune cell subsets from blood, as determined by flow cytometry. (*D*) Serum cytokine levels of CCL2, TNF-α, and IFN-γ, as measured by multiplex analysis. L.O.D., limit of detection. (*E*) Representative gating of CD45$^+$ cells isolated from brain homogenates of PBS-treated or *T. gondii*-infected mice. (*F*) Frequencies of Ly6C^{hi} or Ly6C^{lo} monocytes in brain at 4 and 6 dpi. (*G*) Dominant immune cell subsets from brain, as determined by flow cytometry. For *B*, *D*, and *F*, each data point represents a single mouse. n = 6 to 9 mice per group from 2 to 3 independent experiments throughout. *$P < 0.05$, **$P < 0.01$, ***$P < 0.001$, ****$P < 0.0001$; significance was calculated by 1-way ANOVA with a Tukey post hoc test. Error bars represent SEM.

No other CD45$^+$ infiltrating populations were detected at a significant level in brain homogenates at 4 and 6 dpi (Fig. 1*G* and *SI Appendix*, Table S2). These results indicate that the mobilization of monocytes into the blood occurred within the first week of acute infection, and there was also a modest but detectable monocyte recruitment to the brain at this time.

Monocyte Recruitment to the CNS Temporally Coincides with the Detection of *T. gondii* in the CNS. To determine immune cell frequencies at later time points, we infected mice with a slightly lower parasite dose to facilitate survival to the chronic stage of infection (>28 d) and assayed monocyte levels in the blood and the brain at 10, 15, and 38 dpi. Although the frequencies of Ly6C^{hi} and Ly6C^{lo} monocytes in the blood was relatively low at these time points (representing less than 1% of CD45$^+$ cells) (Fig. 2*A*), both subsets of monocytes were significantly increased in the CNS, particularly at 15 dpi (32.8 ± 4.99% Ly6C^{hi} and 12.22 ± 1.88% Ly6C^{lo} cells as a percentage of total CD45$^+$ cells) compared to control mice (0.09 ± 0.02% Ly6C^{hi} and 0.31 ± 0.06% Ly6C^{lo}) (Fig. 2*C*). At 10 and 15 dpi, T cell frequencies increased 1.5- and 1.8-fold in the blood of infected compared to control mice (Fig. 2*B* and *SI Appendix*, Table S1), and T cells were detectable in brain homogenates by 15 dpi and persisted at 38 dpi (Fig. 2*D* and *SI Appendix*, Table S2). These data are consistent with prior literature demonstrating the importance of T cell recruitment to the CNS for control of chronic *T. gondii* infection (18). TNF-α and IFN-γ were elevated 14- and 1,895-fold at 10 dpi, followed by a decline at 15 and 38 dpi (Fig. 2*E*). In contrast, CCL2 levels in the sera were similar in control and *T. gondii*-infected mice at these time points. These data revealed that both populations of monocytes were robustly recruited to the CNS by 15 dpi.

We next determined if the monocyte infiltration temporally coincided with the arrival of *T. gondii* in the brain. Parasite burden in the CNS was assessed by flow cytometry using the constitutive GFP expressed by the parasite. By gating on GFP$^+$ events in the brain homogenates of infected mice (Fig. 3*A*), we found low but detectable levels of *T. gondii* in the CNS, which peaked at 15 dpi (457 ± 85 parasite-infected cells per brain) and persisted during chronic infection (211 ± 74 parasite-infected cells per brain) (Fig. 3*B*). We also examined brain sections from control mice and from mice at 15 and 38 dpi by confocal microscopy. GFP$^+$ *T. gondii* were present in the brain at 15 dpi (Fig. 3*C*). In addition, in brain sections from chronically infected mice at 38 dpi, we detected GFP$^+$ chronic-stage bradyzoites within cysts, which were confirmed using antibodies against the cyst wall protein CST-1 (Fig. 3*C*). Taken together, these data demonstrate that *T. gondii* were detectable in the CNS within the same time frame that monocyte recruitment to the CNS was observed.

Monocytes Accumulate at the BBB before Transmigrating into the Parenchyma in *T. gondii*-Infected CCR2$^{RFP/+}$CX3CR1$^{GFP/+}$ Mice. In addition to the expression of Ly6C, monocyte subsets in mice can be identified by their differential expression of the chemokine receptors CX3CR1 and CCR2. Ly6C^{hi} inflammatory monocytes are CCR2^{hi}CX3CR1^{lo}, whereas Ly6C^{lo} patrolling monocytes are CCR2^{lo}CX3CR1^{hi}. To evaluate the localization of immune infiltrating cells to the CNS, we analyzed CCR2$^{RFP/+}$CX3CR1$^{GFP/+}$ mice (25) during *T. gondii* infection. Low-dose infection of these reporter mice revealed that they had similar weight loss (*SI Appendix*, Fig. S1*A*) and survival (*SI Appendix*, Fig. S1*B*) as wild-type (WT) mice. To confirm that the reporter mice expressed the fluorescent reporters in the target monocyte populations, we harvested blood cells from acutely infected CCR2$^{RFP/+}$CX3CR1$^{GFP/+}$ mice and evaluated their RFP and GFP expression using Amnis imaging flow cytometry. As expected, CD11b$^+$Ly6C^{lo} cells expressed cytosolic GFP, indicating CX3CR1 expression, and CD11b$^+$Ly6C^{hi} cells expressed cytosolic RFP, indicating CCR2 expression (Fig. 4*A*). The use of these mice also confirmed that the gating strategy described above did indeed distinguish between the 2 reported subsets of monocytes in mouse brains. Finally, we determined that both inflammatory and patrolling monocyte subsets were recruited to the CNS by 15 dpi in the reporter mice (Fig. 4*B*), as in WT mice (Fig. 2*C*).

To visualize the localization of monocytes in the brain, we infected the CCR2$^{RFP/+}$CX3CR1$^{GFP/+}$ reporter mice with non-fluorescent *T. gondii* or injected PBS as a control, and the brains were harvested for sectioning and evaluation by confocal immunofluorescence microscopy. We stained for the extracellular matrix protein collagen-IV and the endothelial surface glucose transporter GLUT-1 to delineate the blood vessels. In control mice, there was no detectable CCR2-RFP cell localization in the brains or the vessels (Fig. 4 *C*, top row). At 10 dpi, the CCR2-RFP cells were predominantly found within the vessel lumen (Fig. 4 *C*, upper middle row). By 15 dpi, the CCR2-RFP cells were packed within vessels and were also detected within the brain parenchyma (Fig. 4 *C*, lower middle row). These findings are particularly interesting given that the mice were perfused with PBS prior to brain harvest, indicating that these cells were likely firmly attached to the vessel wall. By 38 dpi, nearly all of the CCR2-RFP cells were found outside of the vessels and formed clustered foci within the brain (Fig. 4 *C*, bottom row). These data indicate that CCR2-RFP cells were recruited to and accumulated within blood vessels before transmigrating into the brain. Although CCR2 is expressed on both monocytes and NK cells (26), the flow cytometry analysis (Fig. 2*D*) and microscopy (*SI Appendix*, Fig. S2) of infected brains at these time points revealed few to undetectable NK cells in the brain, indicating that the majority of the detected CCR2-RFP cells were monocytes. In these reporter mice, the patrolling monocytes are GFP$^+$RFP^{lo}, and the microglia are GFP^{hi}RFP$^-$. We noted that regions with CCR2-RFP cell infiltration appeared to have increased numbers of GFP^{hi} cells with the morphology of activated microglia and strong positive staining for the myeloid marker IBA-1 (*SI Appendix*, Fig. S3). Quantification of micrographs from the isocortex of infected animals confirmed that GFP^{hi} cells were indeed more numerous in infected mice than in control mice at 15 dpi and 38 dpi, particularly in areas with high monocyte density (Fig. 4*D*), suggesting a correlation between monocyte infiltration in the CNS and increased numbers of microglia at these sites. Notably, there was not increased cell death in regions of high monocyte accumulation compared to regions with fewer monocytes (*SI Appendix*, Fig. S4).

CCR2-RFP Inflammatory Monocytes Exhibit Dynamic Motility at the BBB during *T. gondii* Infection. The leukocyte adhesion cascade has been well studied in the periphery, and a coordinated regulation of cell-adhesion molecules mediates monocyte recruitment and diapedesis in tissues (27). In contrast, less is known about the dynamics of myeloid cell recruitment in a barriered tissue like the brain, and particularly in response to an infection in the CNS. We investigated the dynamics of this process using 2-photon intravital microscopy at the BBB. To this end, cranial windows were installed in CCR2$^{RFP/+}$ mice, allowing for repeated imaging of monocytes within and outside of blood vessels in the brain in the same fields-of-view (FOV) over multiple days after infection. Mice were infected with *T. gondii* or injected with PBS as a vehicle control, and imaging was performed 50 to 100 μm below the meningeal surface every 3 to 4 d between day 0 and 21 post-infection (Fig. 5*A*). To record the full spectrum of monocyte motility in the vasculature, we performed time-lapse imaging at a fast frame rate (40 frames per second) to capture cells moving at the rate of blood vessel flow and at a slower frame rate (4 frames per second) as a 25-μm *z*-stack to capture slower rolling and crawling motility. Using this strategy, we observed

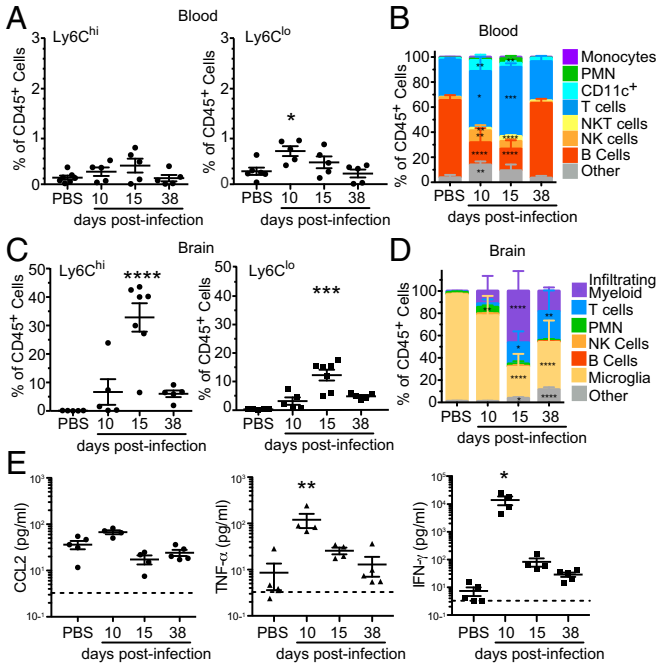

Fig. 2. Monocytes are robustly recruited to the brain during the transition between acute and chronic infection. C57BL/6J mice were infected intraperitoneally with 200 type II *T. gondii* or injected with PBS as a control and analyzed for immune cells in the blood and brain by flow cytometry. Sequential gating strategies shown in Fig. 1 were used. (*A* and *C*) Frequencies of Ly6C^{hi} or Ly6C^{lo} monocytes in blood (*A*) or brain homogenates (*C*) at 10, 15, and 38 dpi. (*B* and *D*) Dominant immune cell subsets in blood (*B*) or brain homogenates (*D*). (*E*) Serum cytokine levels of CCL2, TNF-α, and IFN-γ, as measured by multiplex analysis. Dotted line indicates the limit of detection. Each data point represents a single mouse. $n = 4$ to 7 mice per group from 2 to 3 independent experiments. *$P < 0.05$, **$P < 0.01$, ***$P < 0.001$, ****$P < 0.0001$; significance was calculated by 1-way ANOVA with a Tukey post hoc test. Error bars represent SEM.

CCR2-RFP cells moving within blood vessels and exhibiting classically defined motility modes identified in the periphery, including rolling, crawling, and free-flow movements (Fig. 5*B* and Movies S1 and S2). Imaging in each mouse was performed in the same FOV over sequential days, and cells were tracked frame-by-frame to assess the mean travel speed for individual cells at each time-point. The majority of cells exhibited very fast movement (>200 μm/s) in control mice and at 0 and 4 dpi in *T. gondii*-infected mice (Fig. 5*C*). By 8 dpi, a slower-moving population of cells was detected specifically in infected mice, with a mean speed of between 30 and 100 μm/s (Fig. 5*C*). Between 8 and 21 dpi, the monocytes in *T. gondii*-infected mice continued to decrease in overall speed, which was not observed in control mice (Fig. 5*D*).

We hypothesized that the slower-moving monocyte population indicated an increase in the frequency of rolling and crawling motility within the population. To examine this possibility, we analyzed each tracked monocyte, binning the cells into different motility modes, similar to previous studies on neutrophil motility (28–30). We found that the percentage of cells exhibiting rolling motility remained consistent between control mice and *T. gondii*-infected mice up to 8 dpi, after which we observed a dramatic increase in the proportion of rolling cells and a corresponding decrease in free-flowing cells in the infected mice (Fig. 6*A*). These data are consistent with the slower population we observed in the mean speed analysis, and which was evident starting at 8 dpi (Fig. 5*C*). The increased rolling cell population persisted from 8 to 18 dpi in the infected mice (Fig. 6*A*). We also observed a marked accumulation of stationary or very slow-moving monocytes within some vessels over time in the *T. gondii*-infected mice. As a result of the densely packed CCR2-RFP cells within these vessels, individual crawling or stationary cells were difficult to distinguish from one another and quantify. To investigate the extent of monocyte accumulation, the area of the blood vessels covered by CCR2-RFP cells was quantified instead. Both endogenous autofluorescence and intravenous injection of albumin-AF-488 were used to delineate blood vessels from the brain parenchyma (Fig. 6*B*), and the percent of the vessel or parenchymal area covered by RFP signal was calculated. This analysis revealed a dramatic accumulation of CCR2-RFP cells within vessels of infected mice beginning at 15 dpi and continuing out to 21 dpi (Fig. 6*C*), consistent with the prior analysis of fixed tissue sections (Fig. 4*C*). In contrast, the accumulation of monocytes within the brain parenchyma of infected mice did not reach statistical detection compared to control mice until 21 dpi, suggesting a delay between cell adhesion at the BBB and extravasation into the brain. Interestingly, we did not observe GFP$^+$ *T. gondii* within our imaging FOV, likely due to the relatively low parasite burden in the brains of mice infected intraperitoneally with only 200 *T. gondii*. We verified that we could indeed detect GFP$^+$ parasites by 2-photon microscopy using our imaging settings, by imaging mice immediately after intravenous infection with a high dose of GFP$^+$ parasites (*SI Appendix*, Fig. S5). Collectively, these data demonstrate significant monocyte recruitment to the CNS within 2 wk of *T. gondii* infection and even in regions where parasites were not immediately detected.

Monocyte Infiltration Is Spatially Correlated with Sites of *T. gondii* Infection. One limitation of 2-photon imaging is the size constraint of the imaging window, which allows visualization of only a small portion of the cortex and may not reflect parasite density or immune infiltration into the brain as a whole. To address the degree of parasite infection and monocyte infiltration throughout the brain, we infected CCR2$^{RFP/+}$ mice with GFP-expressing *T. gondii* and prepared the brains for volumetric light-sheet imaging, which enables whole-brain 3D visualization of monocyte localization. Intact brains were harvested at 15 dpi and stained with antibodies against RFP and GFP to label CCR2-RFP monocytes or GFP$^+$ *T. gondii*, respectively. Brains from PBS-injected mice were used to control for nonspecific anti-RFP or anti-GFP antibody staining during tissue processing. LPS injection of a separate cohort of mice was used as an additional control, as described in detail below.

The brains were rendered optically transparant using iDISCO$^+$ and imaged at submicron resolution with a LSFM (31). Tissue autofluorescence in the GFP channel was used to delineate the structure of the brain tissue (Fig. 7 *A*, *Top*). RFP signal consistent with monocyte morphology was observed in all *T. gondii*-infected mice, whereas PBS control mice had no specific RFP signal (Fig. 7 *A*, *Middle*). An automated machine-learning pipeline was developed and validated (*SI Appendix*, Fig. S6) to segment and quantify individual monocytes, each depicted as a unique color (bottom row of Fig. 7 *A* and *B*, and Fig. 7*C*). In *T. gondii*-infected mice, we found hot-spot clusters of monocytes distributed throughout the brain, compared to a more diffuse overall pattern of monocytes in the brains of LPS-treated mice (Fig. 7 *A*, *Middle*, and *SI Appendix*, Fig. S7).

To evaluate if monocyte accumulation was spatially correlated to *T. gondii*, we identified clusters of GFP$^+$ signal colocalizing with signal for the anti-GFP antibody that was used to stain the intact brains. These clusters were also segmented via a custom analysis pipeline (Fig. 7 *B*, *Top*), and the distance of each monocyte to the nearest *T. gondii* cluster was measured in 3D (Fig. 7*D*). Interestingly, monocyte infiltration was significantly enriched near *T. gondii* clusters, with >50% of monocytes found

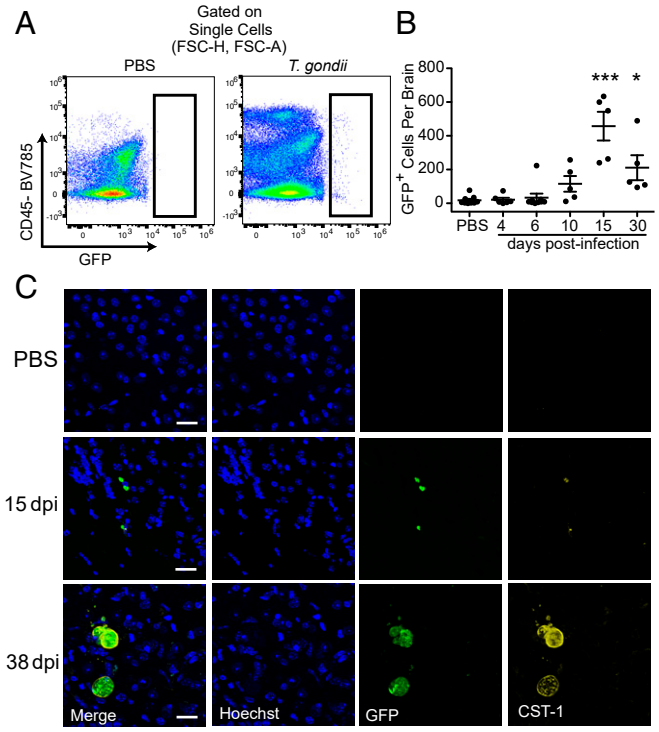

Fig. 3. *T. gondii* enter the brain and are detected during chronic infection. C57BL/6J mice were infected with type II GFP-expressing *T. gondii* parasites or injected with PBS as a control. (*A* and *B*) Brain homogenates were analyzed by flow cytometry, and total numbers of GFP$^+$ (*T. gondii*-infected) cells were plotted. $n = 5$ to 9 mice per group from 2 to 3 independent experiments. $^*P < 0.05$, $^{***}P < 0.001$; significance was calculated by 1-way ANOVA with Tukey post hoc test. Error bars represent SEM. (*C*) Representative confocal microscopy of brain sections from mice at 15 and 38 dpi. Sections were stained with Hoechst to detect nuclei and anti–CST-1 antibody for the *T. gondii* cyst wall. (Scale bars, 25 μm.)

within 300 μm of GFP$^+$ clusters (Fig. 7 *E* and *F*, red lines), and >20% of monocytes within 75 μm of *T. gondii* clusters. To evaluate if this spatial relationship was nonrandom, all of the monocytes in each brain were randomly shuffled and redistributed across the brain, and the distance analysis was reperformed (Fig. 7 *E* and *F*, gray lines). Based on this shuffle analysis, monocytes randomly distributed in the brain were located significantly farther from GFP$^+$ clusters, with <30% of monocytes within 300 μm of *T. gondii* and <7.5% of monocytes within 75 μm. These data indicate that there is a highly significant spatial relationship between monocytes and sites of *T. gondii* infection in the brain, which is likely not a random event.

Whole-Brain Analysis Reveals Regional Specificity of Monocyte Localization. Given the focal nature of *T. gondii*-induced CCR2-RFP monocyte infiltration to the brain, we next asked whether monocytes were recruited to specific regions of the brain during *T. gondii* infection. To do this, the monocyte segmentation data from the brains of the PBS control or *T. gondii*-infected mice were computationally aligned with the Allen Institute annotated brain reference atlas (32). The brain-wide pattern of monocyte infiltration was evaluated using an updated version of ClearMap (31) to quantify the distribution of cells in regions denoted by the Allen reference atlas (32). Three-dimensional heat maps of monocyte density were then generated for each *T. gondii*-infected mouse brain (*SI Appendix*, Fig. S7 and Movie S3). The mean heatmap of monocyte density is shown along with the reference annotation at 2 different sagittal sections in the brain (Fig. 8*A* and Movie S3) (31).

To determine whether the infiltrating monocytes were localized in specific regions of the brain, we compared the density of monocytes in each brain region of *T. gondii*-infected mice against a bootstrapped estimate of expected variance by region. The average monocyte density per region after this shuffle analysis is indicated by the black line in Fig. 8*B*. By analyzing a total of 692 brain regions from the Allen annotated reference atlas (32), 68 regions were found to have an underrepresentation of monocytes compared to the random shuffle analysis (*SI Appendix*, Table S4). Because many of these regions represent cortical layers and divisions of larger functional regions, individual cortical layers and regions differentiated by anatomical location (e.g., anterior/posterior) were collapsed for visualization (Fig. 8*B*, blue bars). The olfactory tubercle was the only region in which there was a significant increase in the detection of CCR2-RFP monocytes across *T. gondii*-infected mice (Fig. 8*B*, brown bar) compared to the shuffle analysis.

We next investigated whether the enrichment of monocytes in the olfactory tubercle was specific to *T. gondii* infection or was also observed in response to a general inflammatory stimulus. To address this question, we administered LPS, a component of gram-negative bacteria and a potent inducer of Toll-like receptor 4 (TLR4) activation, to mice and examined monocyte infiltration to the brain. LPS was injected intraperitoneally into CCR2$^{RFP/+}$ mice at $t = 0$, 24, and 48 h. The brains were harvested at $t = 72$ h, immunostained, and optically cleared identically to the brains from the PBS control and *T. gondii*-infected mice. The cell segmentation algorithm was then used to identify individual monocytes in the brains of LPS-injected mice (Fig. 7 *A*, *Bottom*), and the mean heatmap of monocyte density is shown (Fig. 8*A*). Notably, the degree of monocyte infiltration in the brains of *T. gondii*-infected compared to LPS-injected brains differed significantly, with *T. gondii* inducing over 5-fold greater monocyte recruitment to the brain than LPS treatment (Fig. 8*B*).

Interestingly, there were no regions identified in the brains of LPS-treated mice in which there was an over- or underabundance of monocytes compared to the shuffle analysis, indicating that LPS did not induce a regionally specific monocyte infiltration to the brain. In comparing the distribution of monocytes in the brains of *T. gondii*-infected and LPS-injected mice, we found that in 304 brain regions, there was no statistically significant difference in the numbers of monocytes recruited in response to each stimulus (Fig. 8 *D*, *Upper*). There were 388 regions into which *T. gondii* induced statistically greater monocyte infiltration than LPS, and 0 regions into which LPS treatment induced statistically more monocytes than *T. gondii* (Fig. 8 *D*, *Upper*). These data may reflect the large difference in monocyte abundance in the brain between the 2 treatments (Fig. 8*C*). To account for this possibility, we normalized the monocyte density in each brain region to the overall density per brain in each condition. After performing this correction, there were 6 regions in which *T. gondii* induced preferential monocyte accumulation compared to LPS-treated mice, whereas 159 regions were unique to LPS treatment (Fig. 8 *D* and *E* and *SI Appendix*, Table S5).

These data indicate that LPS induced diffuse monocyte recruitment across the brain, whereas *T. gondii* infection resulted in highly regional monocyte infiltration. Most notably, the olfactory tubercle emerged not only as a region in which monocytes were overrepresented in *T. gondii*-infected mice compared to the shuffle analysis (Fig. 8*B*), but also as a region specific to *T. gondii* infection when compared to LPS treatment (Fig. 8*E*). Other brain regions involved in a diverse set of functions were also overrepresented in monocyte distribution in the *T. gondii*-infected mice compared to LPS injection (Fig. 8*E* and *SI Appendix*, Table S5). Taken together, these data reveal a previously unappreciated and highly specific regional localization of monocytes during the initial recruitment of these cells to the

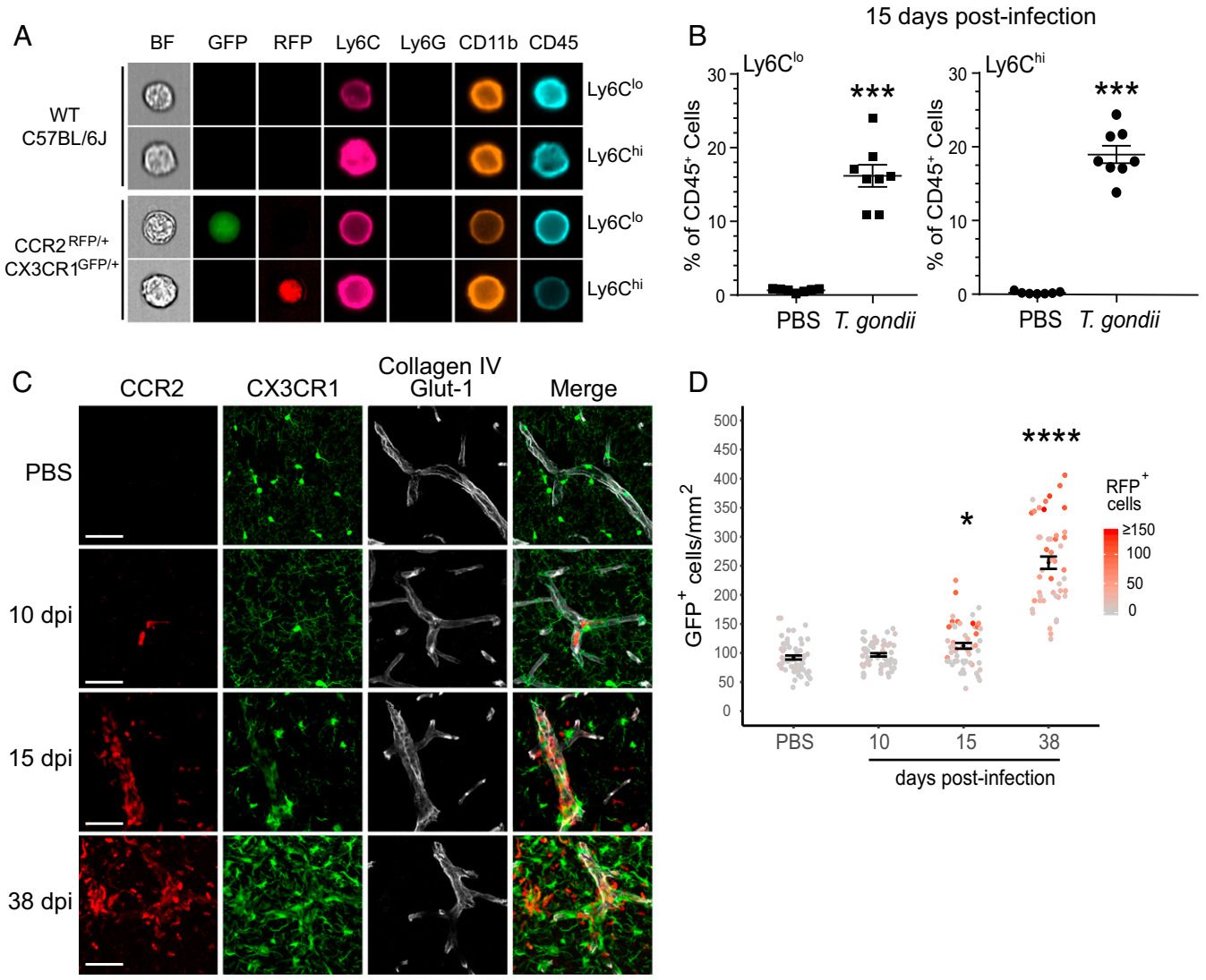

Fig. 4. Monocytes accumulate in the brain vasculature prior to entry to the CNS. WT C57BL/6J mice and $CCR2^{RFP/+}CX3CR1^{GFP/+}$ mice were infected with *T. gondii* or injected with PBS as a control. (*A*) Representative ImageStream analysis of blood cells from $CCR2^{RFP/+}CX3CR1^{GFP/+}$ mice stained with antibodies against Ly6C, Ly6G, CD11b, and CD45. (Magnification, 60×.) (*B*) $Ly6C^{hi}$ and $Ly6C^{lo}$ monocytes from brain homogenates of $CCR2^{RFP/+}CX3CR1^{GFP/+}$ mice infected with nonfluorescent *T. gondii* or injected with PBS as a control. Each data point represents a single mouse. $n = 7$ to 8 mice per group from 2 independent experiments. $***P < 0.001$; significance was calculated by Student's *t* test. Error bars represent SEM. (*C*) Representative confocal images of brain sections from $CCR2^{RFP/+}CX3CR1^{GFP/+}$ mice that were injected with PBS or infected with *T. gondii* at 10, 15, or 38 dpi. Antibodies against collagen IV (extracellular matrix) and Glut-1 (endothelial cells) were used to delineate blood vessels. (Scale bars, 50 μm.) (*D*) $CX3CR1\text{-}GFP^{hi}$ and CCR2-RFP cells were counted from 20× confocal images in the isocortex. Data reflect cells from 18 to 20 FOV per mouse from 3 mice per time point. Each dot represents the number of $CX3CR1\text{-}GFP^{hi}$ cells per square millimeter, and the red intensity of the dots indicates the numbers of CCR2-RFP cells in the same area. $*P < 0.05$, $****P < 0.0001$; significance was calculated by 1-way ANOVA. Error bars represent SEM.

CNS in response to parasite infection and not generalizable to CNS inflammation.

Discussion

T. gondii infection provides a compelling model for investigating the recruitment of inflammatory immune cells to the CNS, both during initial pathogen neuroinvasion and during the chronic stage of the disease when the parasites are encysted in neurons in the brain. Mice are a natural host of *T. gondii*, and survival beyond the acute stage of infection relies on an intact innate immune response involving myeloid cells, as well as robust adaptive immunity (33). Previous work has indicated an essential role for $CCR2^{+}Ly6C^{hi}$ monocytes in host defense during acute infection in peripheral sites (20–22, 34) and in the CNS during chronic stage infection (23). Here, we present a detailed analysis of the dynamic recruitment of monocytes to the CNS during *T. gondii* infection, with a focus on the kinetics and localization of the cells during this process.

Monocytes enter the CNS during many neuroinflammatory conditions, including viral infections and autoimmune diseases, and their role in protection or pathology varies depending on the disease. During West Nile virus infection, the depletion of monocytes in the periphery prevents their entry to the CNS and increases the survival of mice (35). In the mouse model of experimental cerebral malaria (ECM), monocytes adhere to and accumulate in large numbers in cerebral vessels and participate in the removal of parasitized red blood cells (pRBCs) (36). It has also been shown that in the ECM model, mice with the greatest accumulation of stationary monocytes in cerebral vessels suffer the most severe neurological symptoms of disease (37). Monocytes

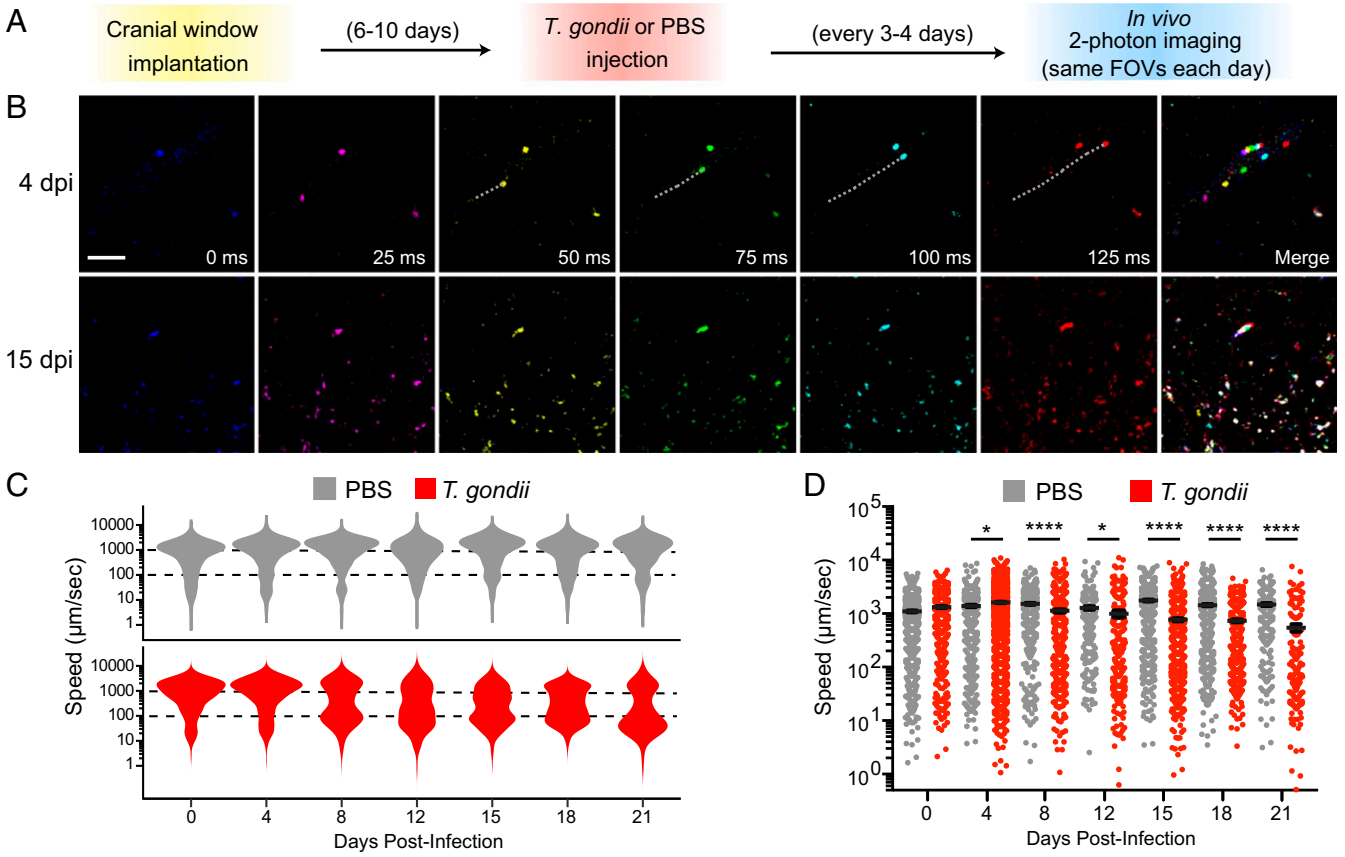

Fig. 5. Monocyte speeds at the BBB decline during infection. CCR2$^{RFP/+}$ mice were infected with *T. gondii* or PBS as a control and imaged by 2-photon microscopy through cranial windows at 0, 4, 8, 12, 15, 18, and 21 dpi to track CCR2-RFP cell movement. Imaging was performed by returning to the same FOV in each mouse each day. (*A*) The experimental design is shown. (*B*) Representative time-lapse imaging of CCR2-RFP cells in vessels and brain parenchyma at 4 and 15 dpi. The RFP signal in each frame was false-colored, and the merged image is shown at right. The track of 1 monocyte at 4 dpi is shown as a dotted white line. (Scale bar, 50 μm.) (*C*) Distribution of CCR2-RFP cell speeds from cell tracking analysis of PBS-injected or *T. gondii*-infected mice from 0 to 21 dpi. (*D*) Speeds of CCR2-RFP cells from PBS or *T. gondii*-infected mice from 0 to 21 dpi. For *C* and *D*, $n_{PBS} > 2{,}000$ cells from 2 to 3 mice per time point, 4 to 5 FOV per mouse. $n_{T.\ gondii} > 2{,}000$ cells from 3 to 5 mice per time point, 4 to 5 FOV per mouse. Error bars represent ± SEM per field. *$P < 0.05$, ****$P < 0.0001$; significance was calculated by 2-tailed *t* test between PBS and *T. gondii* groups at each time point. Significance across the time course was calculated by comparing the slope of the curves for PBS and *T. gondii*-infected mice from 0 to 21 dpi, as determined by linear regression, and performing a Student's *t* test to compare the 2 groups.

may also facilitate cross-talk with CD8$^+$ T cells at the BBB and enhance T cell infiltration of the CNS (37). In ECM, accumulated CD8$^+$ T cells colocalize with pRBCs, leading to vascular leak (38). During *T. gondii* infection, our 2-photon and light-sheet microscopy data revealed vessels with substantial monocyte adhesion in mice without overt clinical signs of disease. One interesting possibility is that the accumulated monocytes observed in *T. gondii*-infected mice may similarly communicate with T cells or facilitate T cell entry to the CNS, potentially contributing to the neuroprotective effect of monocytes during *T. gondii* infection.

Although *T. gondii* infection is largely asymptomatic, it is intriguing that an enrichment of monocytes was detected in a brain region associated with the behavioral changes observed in mice during *T. gondii* infection, which was not found in LPS-induced inflammation. The olfactory tubercle receives direct input from the olfactory bulb and plays a key role in odor-guided behavior. Rodents that are chronically infected with *T. gondii* lose their innate aversion to feline odor and are instead attracted to the odor (39). This effect may be enhanced by certain strains of the parasite (40). Although *T. gondii* replicates asexually in most organisms, cats serve as the definitive host of *T. gondii* by supporting genetic recombination of the parasite. The diminished fear of cat urine by rodents infected with *T. gondii* was proposed as evidence in support of the behavioral manipulation hypothesis (39). Whether the infiltration of monocytes or other immune cells to the olfactory tubercle contributes to the loss of the feline fear response remains to be determined and would be an interesting future avenue of study. Notably, however, the loss of innate aversion to cat urine odors was found to persist even after parasite expansion and inflammation subside in the brain (41).

T. gondii enters the brain by breaching the BBB (42), and long-term survival of mice with chronic *T. gondii* infection requires a robust adaptive immune response, largely mediated by CD4$^+$ and CD8$^+$ T cells in the CNS (18). Reactivation of dormant parasites in the absence of T cells can result in CNS tissue damage as parasites rapidly replicate within and lyse out of sensitive cells. Production of IFN-γ, perforin, and direct cytotoxic lysis of parasite-harboring cells can all contribute to the T cell-mediated protection (43–45). Early recruitment of T cells appears to be mediated at least in part by chemokines such as CXCL9, in addition to VCAM-1 expression by activated endothelial cells (46–48). CXCL10 signals in the brains of chronically infected mice are also required to maintain antigen-specific CD8$^+$ T cells in the brain (49). Interestingly, intravital imaging of T cells in the brain during chronic infection reveals T cell homing to foci of replicating parasites, but no apparent contact

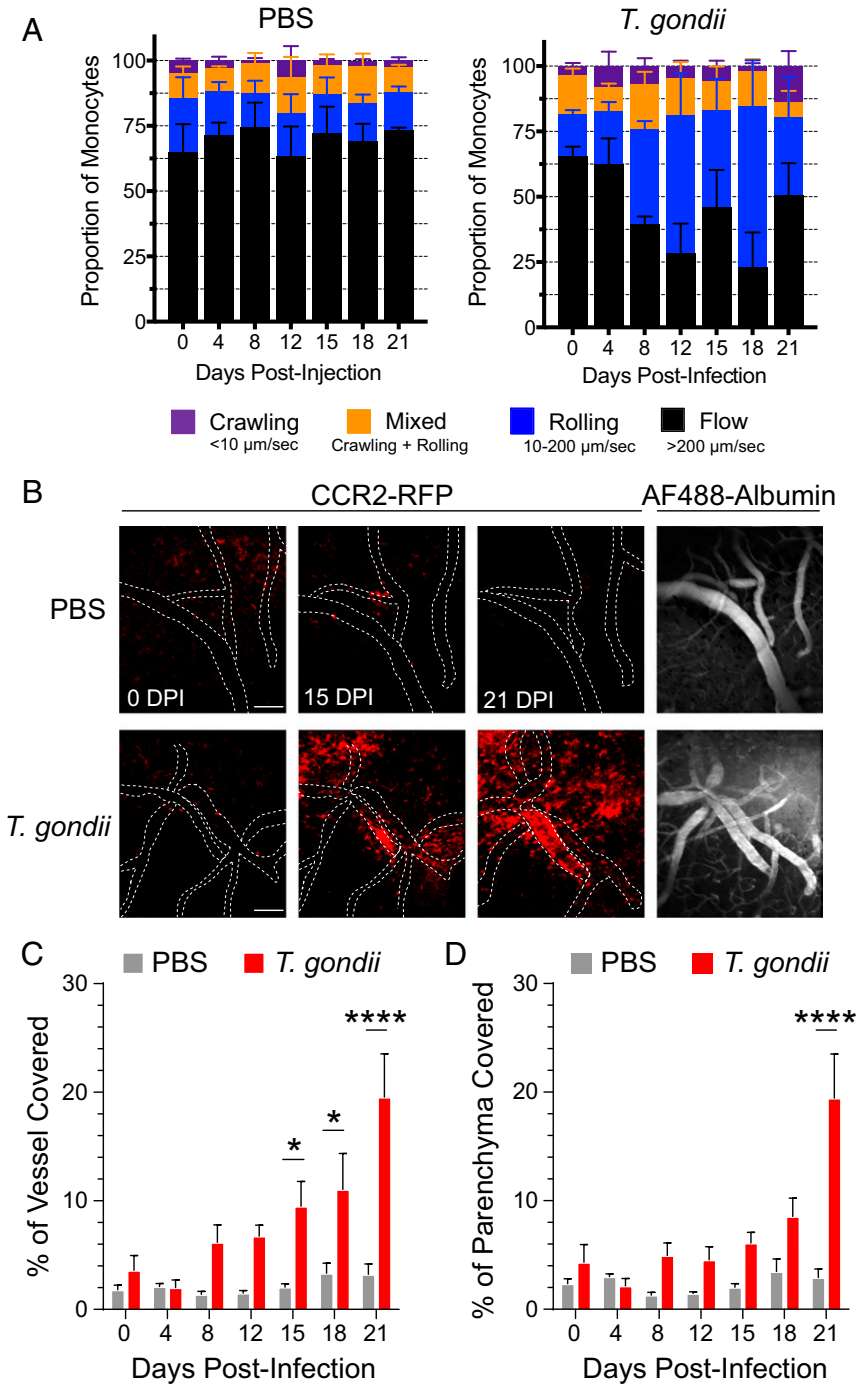

Fig. 6. Infection increases rolling, crawling, and adhesion of monocytes at the BBB. (*A*) Motility of individual tracked monocytes was classified based on speed and presented as a proportion of all monocytes. $n_{PBS} > 2{,}000$ cells from 2 to 3 mice per time point, 4 to 5 FOV per mouse. $n_{T.\ gondii} > 2{,}000$ cells from 3 to 5 mice per time point, 4 to 5 FOV per mouse. (*B*) Representative accumulation of CCR2-RFP cells with overlaid vessel traces (dotted lines) based on either tissue autofluorescence or intravenous injection of Alexa Fluor (AF) 488-Albumin. (Scale bars, 100 μm.) (*C*) Vessel accumulation was quantified as the area covered by CCR2-RFP fluorescence signal over the total area, inside and outside of the vessel boundaries ($n = 3$ to 4 mice per condition per time point with 3 FOV per mouse). $^*P < 0.05$, $^{****}P < 0.0001$; significance was calculated by 2-way ANOVA with a Sidek post hoc test.

with cysts or cyst-bearing cells (50). We observed the majority of monocytes within 300 μm of clusters of *T. gondii* in the brain, suggesting monocytes may be recruited through a parasite-induced process, such as cellular damage or cytokine release from infected cells.

Notably, monocytes were also detected in regions at greater distances from the parasites. These regions may reflect areas in which *T. gondii* existed at some point during the infection but were either cleared by antimicrobial mechanisms or migrated away. Indeed, it has been well documented that the parasites interact with a significantly larger percentage of resident brain cells than those they infect (51). Due to the relatively small number of *T. gondii* clusters, we could not accurately define regionalized trends for parasite localization. However, this brain-wide

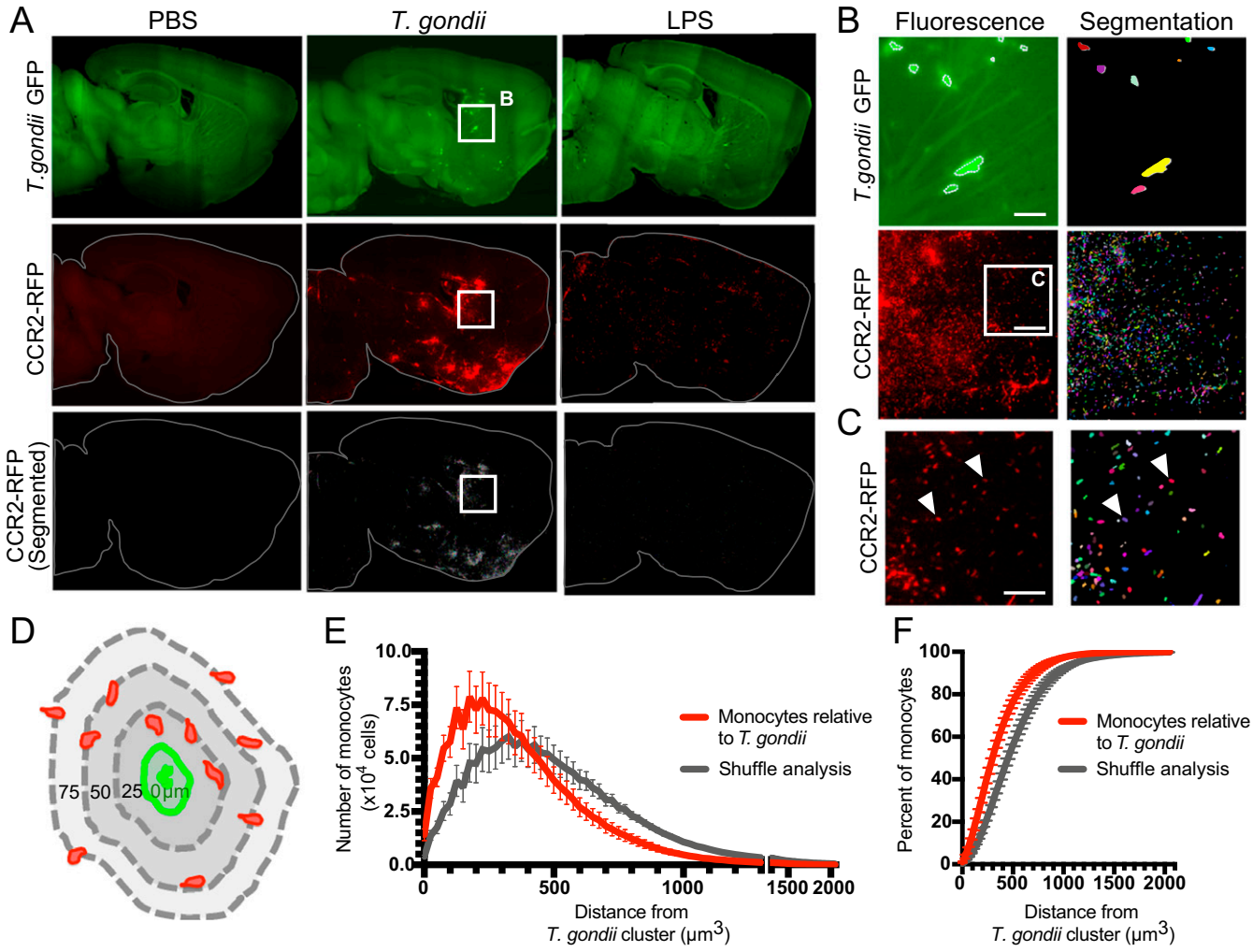

Fig. 7. Monocytes are spatially correlated to *T. gondii* clusters. Brains from CCR2$^{RFP/+}$ mice injected with PBS, *T. gondii*, or LPS were optically cleared using iDISCO^{+} and imaged by light-sheet microscopy. (*A*) Representative optical sections of GFP autofluorescence, GFP^{+} *T. gondii*, CCR2-RFP monocytes, and segmented (individually labeled) CCR2-RFP cells are shown. Contrast adjustment was matched between brains. (*B*) GFP^{+} *T. gondii* and CCR2-RFP cell segmentation show parasite clusters and individual monocytes (each denoted with a different color). (Scale bars, 100 µm.) (*C*) Magnified image of the CCR2-RFP panel in *B*, with white arrowheads indicating individual cells as identified by the segmentation algorithm. (Scale bars, 50 µm.) (*D*) Monocyte distance from each *T. gondii* cluster was measured in 3D space, as depicted. (*E*) Brain-wide analysis of monocyte distance from *T. gondii* clusters (red). Monocytes found within a *T. gondii* cluster have a distance of 0. Monocytes were randomly shuffled and distances of randomly distributed monocytes to *T. gondii* clusters were determined (gray). $P < 10^{-7}$, Kolmogorov-Smirnov test. (*F*) The percent of monocytes at defined distances from *T. gondii* clusters is shown. Error bars represent SEM. n_{PBS} = 5 mice, $n_{T.\ gondii}$ = 5 mice.

regional analysis may be more feasible for examining brain cells with which the parasites have interacted but not necessarily invaded, since these parasite-interacted cells are far more abundant than the parasites alone (52). Indeed, neurons with which the parasites have interacted appear to be enriched in the isocortex and striatum (53). Finally, there may be other, as yet undetermined, signals that induce monocyte infiltration into the brain as a consequence of *T. gondii* infection but not as a direct response to the invading parasites.

In chronic *T. gondii* models, Ly6C^{hi} monocytes infiltrating the CNS do not express classic markers of phagocytic cells, such as TREM2 and F4/80 (23, 54), although it has been shown that Ly6C^{hi} cells can differentiate into more phagocytic Ly6C^{lo} cells, with the potential to contribute directly to parasite clearance (23, 55). Ly6C^{hi} cells were detected in both the hippocampus and the cortex during chronic infection (23, 55). Additionally, in a mouse model of Alzheimer's disease, chronic *T. gondii* infection resulted in increased clearance of plaque-forming Aβ, an outcome attributed to the phagocytic contribution of Ly6C^{hi} monocytes (54). Chronic *T. gondii* infection has also been correlated with decreased memory loss and increased neuron survival in a separate model of Alzheimer's disease (56). In mouse models of multiple sclerosis, T cells are thought to play a dominant role in neuronal demyelination and exacerbating clinical symptoms; however, monocytes have also been shown to infiltrate the CNS and contribute to demyelination, as CCR2 deficiency reduces monocyte recruitment to the CNS and leads to modest improvements both in myelin coverage and clinical score (57).

Collectively, the data presented here represent a comprehensive quantitative analysis of the mobilization of monocytes into the blood and to the CNS during infection. These findings demonstrate the accumulation of monocytes at the BBB and reveal the dynamics of monocyte motility at the BBB in mice analyzed longitudinally from acute to chronic *T. gondii* infection. Moreover, we report a global 3D analysis of monocyte localization in intact brains during infection and LPS-induced inflammation. This analysis provides insight about monocyte activity in the CNS and raises intriguing possibilities about the regional specificity

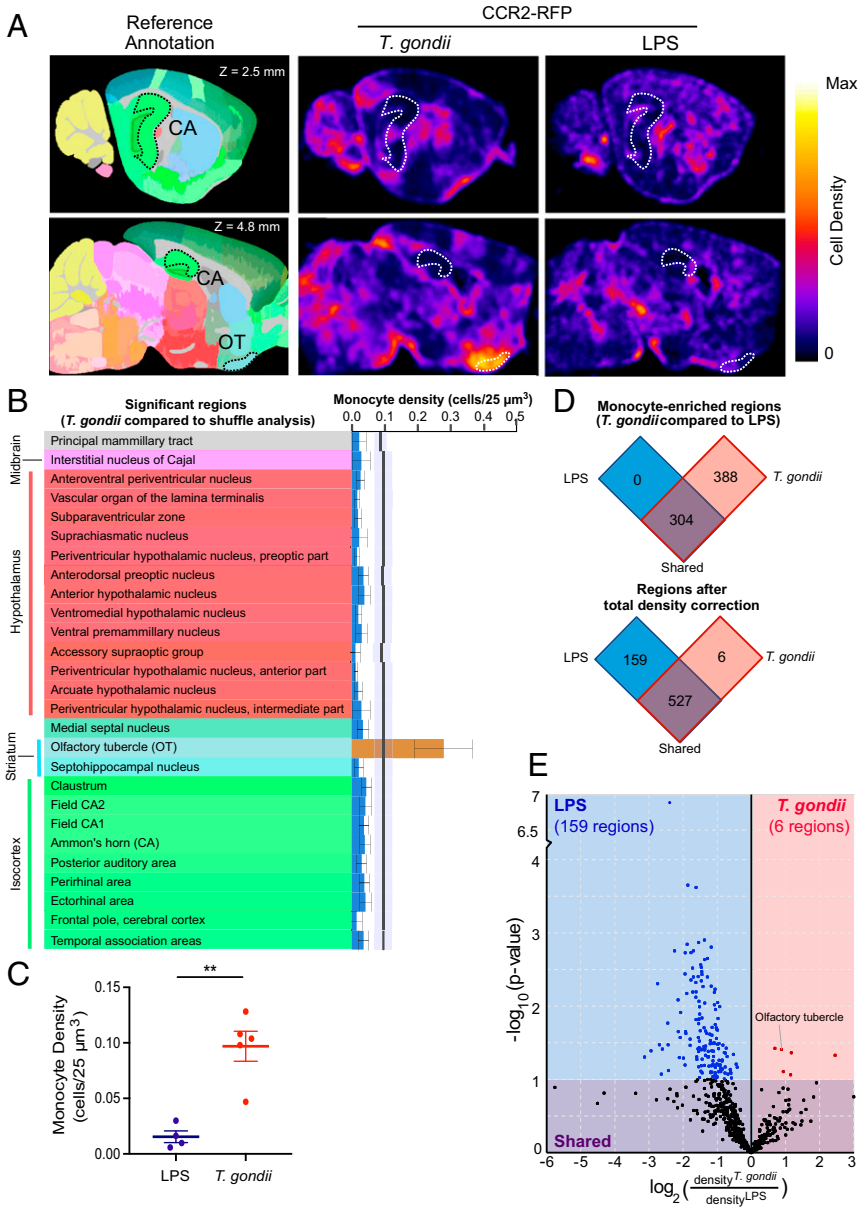

Fig. 8. Brain-wide monocyte localization during *T. gondii* infection and LPS-induced inflammation. Monocyte signal from CCR2$^{RFP/+}$ mouse brains was regionalized by alignment with the mouse reference atlas (Allen Brain Institute). (*A*) Allen reference annotation is shown with CA (Ammon's horn) and OT (olfactory tubercle) outlined (*Left*). Mean density heatmaps of monocyte distribution at 2 different sagittal sections were constructed using all of the brains from the *T. gondii*-infected and LPS-injected mice (*Right*). Heatmaps are normalized to the maximum density within each brain. (*B*) CCR2-RFP monocyte density by brain region in the Allen annotated reference atlas. The black line indicates the shuffle mean, with the corresponding SD in pale blue. Regions with significantly decreased (blue bars) or increased (brown bar) monocyte infiltration compared to the shuffle are shown. Error bars reflect the SD. (*C*) The total monocyte density per 25 μm^3 area was calculated for *T. gondii*-infected and LPS-injected mice. (*D*) Regionalized monocyte density was compared between *T. gondii*-infected and LPS-injected mice without (*Upper*) and with (*Lower*) a normalization for total monocyte density per brain. (*E*) Brain regions enriched for monocytes in LPS-injected or *T. gondii*-infected mice (after total monocyte brain density correction) and their *P* values are shown. Parametric statistics followed by Benjamini–Hochberg correction for false-discovery rate (0.1) was used (*B*, *D*, and *E*). A Welch's *t* test was used for (*C*). $^{**}P < 0.005$. $n_{T.\ gondii} = 5$ mice and $n_{LPS} = 4$ mice.

of immune cell infiltration of the CNS and functional behavioral or pathological outcomes during infection.

Materials and Methods

Mouse Experiments. All procedures and protocols were approved by the Institutional Animal Care and Use Committee at the University of California, Irvine. Two- to 4-mo-old male and female mice were used throughout. Details of mouse strains and breeding are included in *SI Appendix*. Mice were infected with *T. gondii* by intraperitoneal injection of 200 or 1,000 GFP-expressing type II *Prugniaud* or ME49 tachyzoites in 200 μL of PBS. Tachyzoites were serially passaged and maintained in human foreskin fibroblasts, as described previously (58). PBS control mice received an equal volume intraperitoneal injection of sterile PBS (Corning). Mice receiving LPS were injected intraperitoneally with 1 mg/kg LPS from *Salmonella enterica* Typhimurium (Sigma) daily for 3 d and killed 24 h after the final injection. At necropsy, mice were sedated with 2.5% Tribromoethanol (Avertin; Sigma-Aldrich) and perfused transcardially with 30 mL 1× PBS (Corning) to remove circulating blood cells as validated by very low detection of CD45^{hi} blood cells in the brains of mock-infected mice (Fig. 1).

Flow Cytometry. Brains were processed to single-cell suspensions using enzymatic digestion with Dispase II (Roche Applied Science) diluted in Hepes-buffered saline, followed by myelin removal using a Percoll gradient (GE

Healthcare). Blood was removed via cardiac puncture into EDTA anticoagulant tubes (Greiner Bio-one). RBCs were lysed using ACK lysis buffer (Life Technologies). Blood and brain cells were resuspended in staining buffer (1× PBS + 3% FBS) with 10% TrueStain FcX (Biolegend) to block nonspecific antibody binding to Fc receptors. Cells were surface-stained with directly conjugated antibodies (*SI Appendix*, Table S3) followed by 15- to 30-min fixation in 2% paraformaldehyde. Samples were analyzed on a NovoCyte flow cytometer (Acea), and the data were analyzed using FlowJo software (Treestar). For imaging flow cytometry, cells were prepared as above but run on an Amnis ImageStream X Mark II imaging flow cytometer (EMD Millipore) and analyzed using IDEAS software (EMD Millipore).

Immunofluorescence Imaging. Brains were removed and placed in 4% paraformaldehyde for 6 to 16 h, cryopreserved in 30% sucrose in PBS until the tissue sank, and embedded in OCT freezing medium (Thermo Fisher Scientific). The 25-μm-thick sections were stored in cryoprotection media (30% sucrose, 30% ethylene glycol, 0.1M Phosphate buffer, 1% PVP-40) at −20 °C or −80 °C. Details of antibody staining can be found in *SI Appendix*. Confocal microscopy was performed on a Leica SP8 microscope (Leica Microsystems). Images were analyzed using FIJI (59) or Imaris (Bitplane). Quantification of microglia and RFP^+ cells is described in *SI Appendix*.

Two-Photon Imaging. The detailed procedure for cranial window implantation is included in *SI Appendix*. Monocyte fluorescence through cranial windows was imaged with a resonant 2-photon microscope (Neurolabware) using 780- to 800-nm excitation light (Mai Tai HP, Spectra-Physics) and a 16× Nikon water immersion lens (0.8 NA). Emissions were filtered using a 510/84-nm and 607/70-nm BrightLine bandpass filter (Semrock). Image sequences were gathered using Scanbox acquisition software (Scanbox) at a depth of 50 to 150 μm below the meninges. Each recording field was imaged twice per time point. First, an electrically tunable lens (Optotune) was used to simultaneously image 5 planes (685 × 682 μm) ∼10 μm apart, each acquired at 4 Hz. To capture fast-moving monocytes, a single plane (900 × 448 μm) was acquired at 40 Hz. Cell speed was tracked manually using Imaris software (Bitplane). Vessels were delineated using native tissue autofluorescence in the GFP channel and tail-vein injection of 200 μg albumin-AF-488 in sterile PBS (Invitrogen). Blinding was done for the 2-photon microscopy experiments and is described in *SI Appendix*.

Whole-Mount Immunostaining and Optical Clearing. Five $CCR2^{RFP/+}$ mice infected intraperitoneally with 200 PA7 parasites and 5 PBS control mice were killed at 15 dpi. In addition, 4 $CCR2^{RFP/+}$ mice were injected intraperitoneally daily with 1 mg/kg LPS from *S. enterica* Typhimurium (Sigma) and killed 24 h following the final injection. All mice were transcardially perfused with PBS and 4% paraformaldehyde. Brains were extracted and placed in 4% paraformaldehyde for 12 to 16 h and washed 3 times in 1× PBS for 1 h each. Brain tissue was treated with the $iDISCO^+$ protocol (31) for whole-mount immunostaining and to render it optically transparent. The standard protocol was observed with the following deviations: A 24-h incubation in 30% MeOH/66% DCM, followed by 2 washes in 100% methanol for 1 h each was done just prior to the 5% H_2O_2 incubation. Before incubation in permeabilization solution, brain samples were cut into 2 pieces 1-mm lateral of the midline. The portion containing the left hemisphere was utilized for subsequent processing. Tissue was incubated with rabbit anti-RFP (Rockland; 1:400) and chicken anti-GFP (Aves; 1:800) in a 2-mL solution for 4 d. For secondary antibody amplification, tissue was incubated with goat anti-chicken Alexa Fluor 647 (LifeTechnologies; 1:400) and goat anti-rabbit Alexa Fluor 568 (LifeTechnologies; 1:400) in 2 mL solution for 4 d.

Light-Sheet Fluorescence Imaging. $iDISCO^+$ treated and immunostained samples were imaged in the sagittal orientation using custom sample holders and a modified imaging chamber designed to accommodate whole-brain samples imaged in Di-Benzyl Ether. Samples were imaged on the Z.1 LSFM (Zeiss) using 5×/0.1NA illumination optics and a 5×/0.16NA detection optic at 1.5× optical zoom. Excitation was done with 488-nm and 638-nm laser lines coupled to BP 505–545, and LP 660 emission filters, respectively. Laser power and exposure was matched across samples and each channel was imaged on a separate track to minimize cross-talk. Illumination was done using only the left sheet optic. Tiling of individual *z*-stacks was done manually using Vision4D (Arivis AG) and correct placement verified by another rater.

Whole-Brain Cell Segmentation Analysis. Analysis was performed using a modified version of ClearMap (31) that was retooled to handle the larger datasets produced by the Z.1 LSFM. A detailed description of the analysis and validation of the cell segmentation classifier is in *SI Appendix*.

***T. gondii*–Monocyte Distance Analysis.** GFP^+ *T. gondii* clusters were identified in the 5 infected $CCR2^{RFP/+}$ mice with segmented monocytes. Data were run through a 5-px median filter then put through a rolling background subtraction with 30-px radius (60) and finally binarized with a threshold of 1 SD above the image mean. Final image data were segmented to identify *T. gondii* clusters. Clusters with size <1,000 px were excluded. Segmented clusters were warped to the Allen reference atlas (32) as described and voxels containing clusters were assigned as belonging to the cluster. For each segmented monocyte in the reference coordinate space, the minimum Euclidian distance, in voxels, to a *T. gondii* cluster was calculated and rounded up to bin the data. The number of cells with each rounded distance was counted. Cells within the clusters were given a distance of zero. Values were multiplied by 25 to convert to cubic micrometers.

Statistical methods for all analyses are described in *SI Appendix*.

Data Availability. The code associated with this paper has been deposited in GitHub: https://github.com/sunilgandhilab/brainquant3d (61).

ACKNOWLEDGMENTS. We thank members of the M.B.L., Tenner, Nelson, Morrissette, Andrade, and Messaoudi laboratories for helpful discussion on this project; Dr. Adeela Syed for her expertise in imaging; Dr. Tuyen Hoang of the Biostatistics, Epidemiology & Research Design Unit of the University of California, Irvine Institute for Clinical and Translational Science; Dr. Robert Spitale and Dr. Whitney England for statistical consultation; and Dr. Kim Green for help with microglia quantification. This work was supported by NIH R01AI120846 (to M.B.L.), American Cancer Society 126688-RSG-14-202-01-MPC (to M.B.L.), NIH 5F30EY029596-02 (to R.A.), 5F31EY028046-03 to (D.X.F.V.), NIH T32GM008620 (to R.A. and E.M.H.), and NIH T32AI060573 (to C.A.S. and E.M.H.). This study was made possible in part through access to the Optical Biology Core Facility of the Developmental Biology Center, a shared resource supported by the Cancer Center Support Grant (CA-62203) and Center for Complex Biological Systems Support Grant (GM-076516) at the University of California, Irvine.

1. N. V. Serbina, T. Jia, T. M. Hohl, E. G. Pamer, Monocyte-mediated defense against microbial pathogens. *Annu. Rev. Immunol.* **26**, 421–452 (2008).
2. F. Ginhoux, S. Jung, Monocytes and macrophages: Developmental pathways and tissue homeostasis. *Nat. Rev. Immunol.* **14**, 392–404 (2014).
3. A. J. Mitchell, B. Roediger, W. Weninger, Monocyte homeostasis and the plasticity of inflammatory monocytes. *Cell. Immunol.* **291**, 22–31 (2014).
4. C. Shi, E. G. Pamer, Monocyte recruitment during infection and inflammation. *Nat. Rev. Immunol.* **11**, 762–774 (2011).
5. C. L. Tsou *et al*., Critical roles for CCR2 and MCP-3 in monocyte mobilization from bone marrow and recruitment to inflammatory sites. *J. Clin. Invest.* **117**, 902–909 (2007).
6. L. Boring *et al*., Impaired monocyte migration and reduced type 1 (Th1) cytokine responses in C-C chemokine receptor 2 knockout mice. *J. Clin. Invest.* **100**, 2552–2561 (1997).
7. T. M. Hohl *et al*., Inflammatory monocytes facilitate adaptive CD4 T cell responses during respiratory fungal infection. *Cell Host Microbe* **6**, 470–481 (2009).
8. F. Geissmann, S. Jung, D. R. Littman, Blood monocytes consist of two principal subsets with distinct migratory properties. *Immunity* **19**, 71–82 (2003).
9. G. J. Randolph, K. Inaba, D. F. Robbiani, R. M. Steinman, W. A. Muller, Differentiation of phagocytic monocytes into lymph node dendritic cells in vivo. *Immunity* **11**, 753–761 (1999).
10. C. Auffray, M. H. Sieweke, F. Geissmann, Blood monocytes: Development, heterogeneity, and relationship with dendritic cells. *Annu. Rev. Immunol.* **27**, 669–692 (2009).
11. C. Auffray *et al*., Monitoring of blood vessels and tissues by a population of monocytes with patrolling behavior. *Science* **317**, 666–670 (2007).
12. M. A. Ingersoll *et al*., Comparison of gene expression profiles between human and mouse monocyte subsets. *Blood* **115**, e10–e19 (2010).
13. K. L. Wong *et al*., Gene expression profiling reveals the defining features of the classical, intermediate, and nonclassical human monocyte subsets. *Blood* **118**, e16–e31 (2011).
14. J. Cros *et al*., Human CD14dim monocytes patrol and sense nucleic acids and viruses via TLR7 and TLR8 receptors. *Immunity* **33**, 375–386 (2010).
15. G. Pappas, N. Roussos, M. E. Falagas, Toxoplasmosis snapshots: Global status of Toxoplasma gondii seroprevalence and implications for pregnancy and congenital toxoplasmosis. *Int. J. Parasitol.* **39**, 1385–1394 (2009).
16. J. P. Saeij, J. P. Boyle, M. E. Grigg, G. Arrizabalaga, J. C. Boothroyd, Bioluminescence imaging of Toxoplasma gondii infection in living mice reveals dramatic differences between strains. *Infect. Immun.* **73**, 695–702 (2005).
17. J. G. Montoya, O. Liesenfeld, Toxoplasmosis. *Lancet* **363**, 1965–1976 (2004).
18. R. Gazzinelli, Y. Xu, S. Hieny, A. Cheever, A. Sher, Simultaneous depletion of CD4+ and CD8+ T lymphocytes is required to reactivate chronic infection with Toxoplasma gondii. *J. Immunol.* **149**, 175–180 (1992).

19. R. S. Goldszmid *et al*., NK cell-derived interferon-γ orchestrates cellular dynamics and the differentiation of monocytes into dendritic cells at the site of infection. *Immunity* **36**, 1047–1059 (2012).
20. I. R. Dunay *et al*., Gr1(+) inflammatory monocytes are required for mucosal resistance to the pathogen Toxoplasma gondii. *Immunity* **29**, 306–317 (2008).
21. I. R. Dunay, A. Fuchs, L. D. Sibley, Inflammatory monocytes but not neutrophils are necessary to control infection with Toxoplasma gondii in mice. *Infect. Immun.* **78**, 1564–1570 (2010).
22. P. M. Robben, M. LaRegina, W. A. Kuziel, L. D. Sibley, Recruitment of Gr-1+ monocytes is essential for control of acute toxoplasmosis. *J. Exp. Med.* **201**, 1761–1769 (2005).
23. A. Biswas *et al*., Ly6C(high) monocytes control cerebral toxoplasmosis. *J. Immunol.* **194**, 3223–3235 (2015).
24. L. Benevides *et al*., CCR2 receptor is essential to activate microbicidal mechanisms to control Toxoplasma gondii infection in the central nervous system. *Am. J. Pathol.* **173**, 741–751 (2008).
25. N. Saederup *et al*., Selective chemokine receptor usage by central nervous system myeloid cells in CCR2-red fluorescent protein knock-in mice. *PLoS One* **5**, e13693 (2010).
26. V. Bianconi, A. Sahebkar, S. L. Atkin, M. Pirro, The regulation and importance of monocyte chemoattractant protein-1. *Curr. Opin. Hematol.* **25**, 44–51 (2018).
27. T. Gerhardt, K. Ley, Monocyte trafficking across the vessel wall. *Cardiovasc. Res.* **107**, 321–330 (2015).
28. E. J. Kunkel, K. Ley, Distinct phenotype of E-selectin-deficient mice. E-selectin is required for slow leukocyte rolling in vivo. *Circ. Res.* **79**, 1196–1204 (1996).
29. U. Jung, D. C. Bullard, T. F. Tedder, K. Ley, Velocity differences between L- and P-selectin-dependent neutrophil rolling in venules of mouse cremaster muscle in vivo. *Am. J. Physiol.* **271**, H2740–H2747 (1996).
30. A. Zarbock, C. A. Lowell, K. Ley, Spleen tyrosine kinase Syk is necessary for E-selectin-induced alpha(L)beta(2) integrin-mediated rolling on intercellular adhesion molecule-1. *Immunity* **26**, 773–783 (2007).
31. N. Renier *et al*., Mapping of brain activity by automated volume analysis of immediate early genes. *Cell* **165**, 1789–1802 (2016).
32. E. S. Lein *et al*., Genome-wide atlas of gene expression in the adult mouse brain. *Nature* **445**, 168–176 (2007).
33. N. Blanchard, I. R. Dunay, D. Schlüter, Persistence of Toxoplasma gondii in the central nervous system: A fine-tuned balance between the parasite, the brain and the immune system. *Parasite Immunol.* **37**, 150–158 (2015).
34. M. H. Askenase *et al*., Bone-marrow-resident NK cells prime monocytes for regulatory function during infection. *Immunity* **42**, 1130–1142 (2015).
35. D. R. Getts *et al*., Ly6c+ "inflammatory monocytes" are microglial precursors recruited in a pathogenic manner in West Nile virus encephalitis. *J. Exp. Med.* **205**, 2319–2337 (2008).
36. P. A. Swanson, 2nd *et al*., CD8+ T cells induce fatal brainstem pathology during cerebral malaria via luminal antigen-specific engagement of brain vasculature. *PLoS Pathog.* **12**, e1006022 (2016).
37. S. Pai *et al*., Real-time imaging reveals the dynamics of leukocyte behaviour during experimental cerebral malaria pathogenesis. *PLoS Pathog.* **10**, e1004236 (2014).
38. P. Strangward *et al*., A quantitative brain map of experimental cerebral malaria pathology. *PLoS Pathog.* **13**, e1006267 (2017).
39. A. Vyas, S. K. Kim, N. Giacomini, J. C. Boothroyd, R. M. Sapolsky, Behavioral changes induced by Toxoplasma infection of rodents are highly specific to aversion of cat odors. *Proc. Natl. Acad. Sci. U.S.A.* **104**, 6442–6447 (2007).
40. G. Kannan *et al*., Toxoplasma gondii strain-dependent effects on mouse behaviour. *Folia Parasitol. (Praha)* **57**, 151–155 (2010).
41. W. M. Ingram, L. M. Goodrich, E. A. Robey, M. B. Eisen, Mice infected with low-virulence strains of Toxoplasma gondii lose their innate aversion to cat urine, even after extensive parasite clearance. *PLoS One* **8**, e75246 (2013).
42. C. Konradt *et al*., Endothelial cells are a replicative niche for entry of Toxoplasma gondii to the central nervous system. *Nat. Microbiol.* **1**, 16001 (2016).
43. Y. Suzuki, F. K. Conley, J. S. Remington, Importance of endogenous IFN-gamma for prevention of toxoplasmic encephalitis in mice. *J. Immunol.* **143**, 2045–2050 (1989).
44. Y. Suzuki *et al*., Removal of Toxoplasma gondii cysts from the brain by perforin-mediated activity of CD8+ T cells. *Am. J. Pathol.* **176**, 1607–1613 (2010).
45. E. Y. Denkers *et al*., Perforin-mediated cytolysis plays a limited role in host resistance to Toxoplasma gondii. *J. Immunol.* **159**, 1903–1908 (1997).
46. E. Ochiai *et al*., CXCL9 is important for recruiting immune T cells into the brain and inducing an accumulation of the T cells to the areas of tachyzoite proliferation to prevent reactivation of chronic cerebral infection with Toxoplasma gondii. *Am. J. Pathol.* **185**, 314–324 (2015).
47. Q. Sa *et al*., VCAM-1/α4β1 integrin interaction is crucial for prompt recruitment of immune T cells into the brain during the early stage of reactivation of chronic infection with Toxoplasma gondii to prevent toxoplasmic encephalitis. *Infect. Immun.* **82**, 2826–2839 (2014).
48. E. H. Wilson *et al*., Behavior of parasite-specific effector CD8+ T cells in the brain and visualization of a kinesis-associated system of reticular fibers. *Immunity* **30**, 300–311 (2009).
49. T. H. Harris *et al*., Generalized Lévy walks and the role of chemokines in migration of effector CD8+ T cells. *Nature* **486**, 545–548 (2012).
50. M. Schaeffer *et al*., Dynamic imaging of T cell-parasite interactions in the brains of mice chronically infected with Toxoplasma gondii. *J. Immunol.* **182**, 6379–6393 (2009).
51. A. A. Koshy *et al*., Toxoplasma secreting Cre recombinase for analysis of host-parasite interactions. *Nat. Methods* **7**, 307–309 (2010).
52. A. A. Koshy *et al*., Toxoplasma co-opts host cells it does not invade. *PLoS Pathog.* **8**, e1002825 (2012).
53. O. A. Mendez *et al*., Semi-automated quantification and neuroanatomical mapping of heterogeneous cell populations. *J. Neurosci. Methods* **305**, 98–104 (2018).
54. L. Möhle *et al*., Chronic Toxoplasma gondii infection enhances β-amyloid phagocytosis and clearance by recruited monocytes. *Acta Neuropathol. Commun.* **4**, 25 (2016).
55. H. P. Düsedau *et al*., $p75^{NTR}$ regulates brain mononuclear cell function and neuronal structure in Toxoplasma infection-induced neuroinflammation. *Glia* **67**, 193–211 (2019).
56. B. K. Jung *et al*., Toxoplasma gondii infection in the brain inhibits neuronal degeneration and learning and memory impairments in a murine model of Alzheimer's disease. *PLoS One* **7**, e33312 (2012).
57. R. Yamasaki *et al*., Differential roles of microglia and monocytes in the inflamed central nervous system. *J. Exp. Med.* **211**, 1533–1549 (2014).
58. L. Gov, A. Karimzadeh, N. Ueno, M. B. Lodoen, Human innate immunity to Toxoplasma gondii is mediated by host caspase-1 and ASC and parasite GRA15. *MBio* **4**, e00255-13 (2013).
59. J. Schindelin *et al*., Fiji: An open-source platform for biological-image analysis. *Nat. Methods* **9**, 676–682 (2012).
60. S. Sternberg, Biomedical image processing. *IEEE Computer* **16**, 22–34 (1983).
61. S. P. Gandhi, Brainquant3d: Terabyte scale tissue analysis software. Github. https://github.com/sunilgandhilab/brainquant3d. Deposited 15 October 2019.